Epitaxial Growth of Branched α-Fe_2O_3/SnO_2 Nano-Heterostructures with Improved Lithium-Ion Battery Performance

Weiwei Zhou, Chuanwei Cheng, Jinping Liu, Yee Yan Tay, Jian Jiang, Xingtao Jia, Jixuan Zhang, Hao Gong, Huey Hoon Hng, Ting Yu, and Hong Jin Fan**

We report the synthesis of a novel branched nano-heterostructure composed of SnO_2 nanowire stem and α-Fe_2O_3 nanorod branches by combining a vapour transport deposition and a facile hydrothermal method. The epitaxial relationship between the branch and stem is investigated by high resolution transmission electron microscopy (HRTEM). The SnO_2 nanowire is determined to grow along the [101] direction, enclosed by four side surfaces. The results indicate that distinct crystallographic planes of SnO_2 stem can induce different preferential growth directions of secondary nanorod branches, leading to six-fold symmetry rather than four-fold symmetry. Moreover, as a proof-of-concept demonstration of the function, such α-Fe_2O_3/SnO_2 composite material is used as a lithium-ion batteries (LIBs) anode material. Low initial irreversible loss and high reversible capacity are demonstrated, in comparison to both single components. The synergetic effect exerted by SnO_2 and α-Fe_2O_3 as well as the unique branched structure are probably responsible for the enhanced performance.

1. Introduction

Growth of complex nanostructures with controllable dimensions has attracted increasing interest due to the fact that diverse properties can be generated by tailoring the morphology, composition, and assembling organization of the primary nanobuilding blocks.[1] In particular, branched nanostructures are more attractive in many nanoscale device applications, for which large surface areas are desirable. For examples, the addition of branches to unidirectional nanowires will improve the light harvesting ability by providing much more surfaces for loading dye molecules or semiconductor quantum dots, as well as light trapping due to multi-scattering, in contrast to a conventional planar device;[2] this may be beneficial to photovoltaic and photoelectrochemical applications.[3] Furthermore, branched nano-heterostructures composed of proper semiconductors would lead to superior photocatalytic abilities owing to the electron-hole separation at the interface arising from the band alignment.[4] Very recently, a novel high capacity anode material for lithium-ion batteries (LIBs) has been developed by forming a quasi-branched nano-heterostructure, utilizing the high conductivity and structural integrity of the inner inactive core to permit reproducible Li^+ insertion and extraction into and from the outer Si coating.[5]

In recent years, various materials like PbS,[6] TiO_2,[1a,7] V_2O_5,[8] SnO_2,[9] Fe_2O_3,[4,10] and techniques including sequential seeding of catalysts and self-assembled growth of nanowires have been demonstrated to form three-dimensional branched,[11] hyperbranched,[6,12] and multibranched nanowire structures.[13] Nevertheless, a control of the size, dimension, and composition of the building blocks of hierarchical nanostructures in an expected manner is still a great challenge. Solution-phase growth generally allows a higher degree of control compared with vapour-phase strategies.[4,14] In addition, the characteristics of low cost, low growth temperature, environmental friendliness, process simplicity, and high yield make solution-based methods very promising.

SnO_2 and α-Fe_2O_3, both important functional materials, have been intensively investigated separately for their applications as photocatalysts,[15] gas sensors,[16] and electrodes.[17] It has been previously demonstrated that a SnO_2/α-Fe_2O_3 hybrid composite can yield enhanced functions like gas sensitivity.[18] Recently, several research groups have assembled SnO_2 nanorod branches onto various α-Fe_2O_3 stems.[4,10] To our best knowledge, there is no report on the reverse structure

W. W. Zhou, Dr. C. W. Cheng, X. T. Jia, Prof. T. Yu, Prof. H. J. Fan
Division of Physics and Applied Physics
School of Physical and Mathematical Sciences
Nanyang Technological University
637371, Singapore
E-mail: hjfan@ntu.edu.sg; yuting@ntu.edu.sg
Dr. Y. Y. Tay, Prof. H. H. Hng
School of Materials Science and Engineering
Nanyang Technological University
639798, Singapore
Dr. J. X. Zhang, Prof. H. Gong
Department of Materials Science and Engineering
National University of Singapore
117576, Singapore
Dr. J. P. Liu, J. Jiang
Institute of Nanoscience and Nanotechnology
Department of Physics
Huazhong Normal University
Wuhan 430079, P. R. China

DOI: 10.1002/adfm.201100088

in which α-Fe_2O_3 nanorod branches grow epitaxially on SnO_2 nanowire stems. In this work, we have successfully prepared six-fold-symmetry branched FeOOH/SnO_2 and α-Fe_2O_3/SnO_2 nano-heterostructures by combining chemical vapour deposition (for the SnO_2 stem) and a hydrothermal route (for the FeOOH branches). The lengths of FeOOH nanorods can be simply tuned by adjusting the concentration of the reactant or the growth time. It should be noted that in previous reports, the six-fold-symmetry branched nano-heterostructures are induced by the anchoring of branches onto six identical surfaces of the stems.[4,10b,11b,19] In our case, surprisingly, the secondary FeOOH nanorods are epitaxially grown on the four side surfaces of the SnO_2 nanowires with a six-fold-symmetry, which is a result of the minimization of lattice mismatches on distinct SnO_2 surfaces. The epitaxial relationship between the branch and the stem is studied by high resolution transmission electron microscopy (HRTEM) in detail. A simple three-step growth process is proposed, based on a series of control experiments. Finally, as both Fe_2O_3 and SnO_2 are important functional materials, a proof-of-concept of the function of such branched α-Fe_2O_3/SnO_2 composites as LIBs anode is demonstrated, which shows that the α-Fe_2O_3/SnO_2 composites have superior performance to both SnO_2 and α-Fe_2O_3 individual components in terms of low initial irreversible loss and high reversible capacity. The synergetic effect between SnO_2 and α-Fe_2O_3 and the characteristic of branched nanostructure are proposed to be the origin of the performance improvement.

2. Results and Discussion

2.1. Structure Characterization, Growth Control, and Mechanism Investigation

XRD patterns in **Figure 1** reveal the overall crystal structure and phase purity of the three as-obtained samples: pristine SnO_2 nanowires, bare α-Fe_2O_3 nanorod arrays, and hierarchical

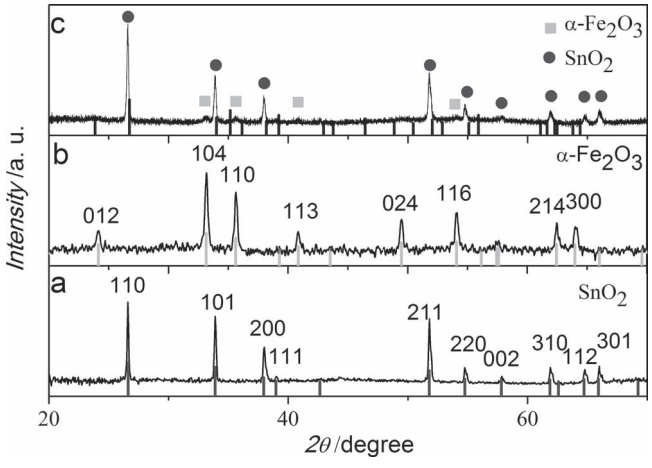

Figure 1. XRD patterns of a): pristine SnO_2 nanowires; b) bare α-Fe_2O_3 nanorod arrays; c) α-Fe_2O_3/SnO_2 branched nanostructures. The vertical lines in (a), (b), (c) denote the standard XRD patterns corresponding to that of rutile SnO_2 (JCPDF: 41–1445), rhombohedral α-Fe_2O_3 (JCPDF: 33–0664), and tetragonal FeOOH (JCPDF: 34–1266).

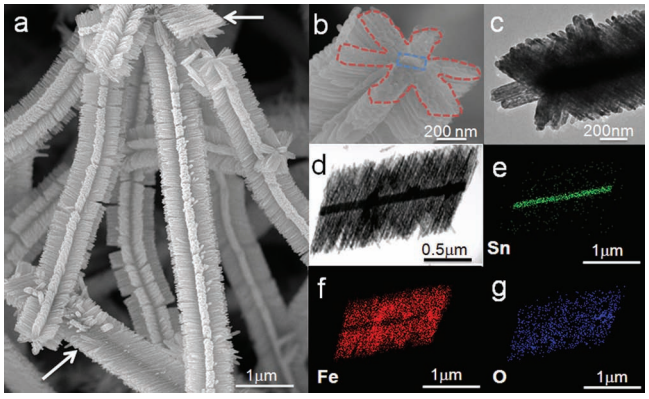

Figure 2. a) Typical SEM image; b, c) High-magnification SEM and TEM images of single six-fold-symmetry branched nanowire. d–g) TEM image of single branched nanowire and the corresponding elemental mapping images.

α-Fe_2O_3/SnO_2 nanostructures, respectively. All the diffraction peaks for the three products match well with those of standard XRD patterns of tetragonal rutile SnO_2 (JCPDF: 41–1445) and rhombohedral α-Fe_2O_3 (JCPDF: 33–0664). Although the positions of some standard XRD peaks of tetragonal FeOOH are very close to those of SnO_2 and α-Fe_2O_3, no additional peaks other than these with similar positions were found in the XRD pattern of α-Fe_2O_3/SnO_2 composites, which is an indication of the complete transition from FeOOH to α-Fe_2O_3.

Figure 2a shows a typical SEM image of the α-Fe_2O_3/SnO_2 composite structures. It demonstrates that the products exhibit hierarchical structures with multiple rows of secondary nanorods grown on the major nanowires in a parallel fashion. In addition, the majority of these hierarchical structures exhibit a six-fold symmetry, i.e., the nanorod branches grow along six directions on the SnO_2 nanowires with the angle of approximately 60° between adjacent branches (Figure 2b). There are also a few two-fold-symmetry structures (indicated by the arrows in Figure 2a), which are considered to be part of the underdeveloped six-fold-symmetry structures. The magnified SEM and TEM images (Figure 2b–d) also reveal that the branches are assembled in bundles of well-aligned porous nanorods. The average diameter and length of the sub-nanorods are estimated to be about 50 nm and length of 500 nm, respectively. The TEM elemental mapping is conducted to clearly identify the spatial distributions of Fe, Sn, and O in the backbone and branches (as shown in Figure 2e–g). In the backbone region, the signals of Sn are strongly detected, while the Fe signals are barely visible. In contrast, the Fe signals are dominant in the branch region, while the Sn signals are nearly absent. The O signals are uniformly distributed over the entire structure as expected.

The length of secondary nanorods can be tuned by varying the reactant concentration. The 500 nm length is achieved from a $FeCl_3$ concentration of 0.15 M (**Figure 3**a), while a half of that concentration can only produce nanorod branches of ~350 nm long (Figure 3b). When the $FeCl_3$ concentration is reduced to 0.037 M, the lengths of the branches are only 70 nm, whereas the six-fold symmetry is still preserved (Figure 3c). With further decreasing the $FeCl_3$ concentration to 0.025 M, only some

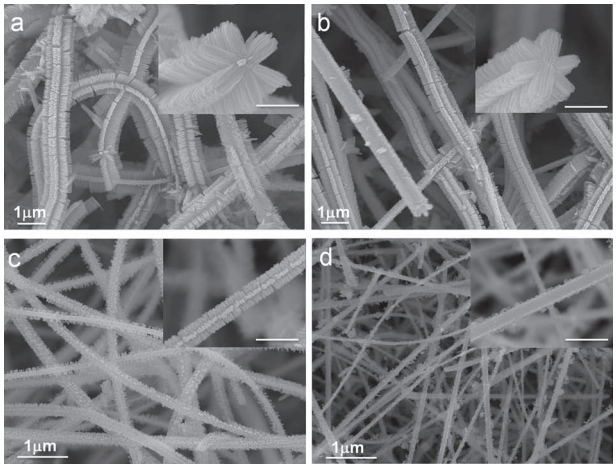

Figure 3. SEM images of the products (after annealing) obtained from different concentrations of $FeCl_3 \cdot 6H_2O$: a) 0.15 M; b) 0.075 M; c) 0.037 M; d) 0.025 M. The insets are the corresponding magnified SEM images. The scale bars in the insets are 500 nm.

nanoparticles and nanoflakes are observed on the surfaces of primary SnO_2 nanowires without any symmetric features (Figure 3d).

The crystallographic relationship between the branch and the stem was investigated in detail by HRTEM imaging of the interface. **Figure 4**a is a TEM image of one as-obtained six-fold-symmetry branched nanowire. The branches are assigned to be FeOOH with a tetragonal structure according to its XRD pattern (JCPDF: 34–1266, Figure S1). Figure 4b is the corresponding HRTEM image of the circled interfacial area in Figure 4a. The lattice spacings of 0.26 nm for the stem and 0.25 nm for the branch are in good agreement with (10–1) and (330) interplanar spacings of tetragonal SnO_2 and FeOOH, respectively. The (330) planes of FeOOH stack parallel to the (10–1) ones of SnO_2, implying that the FeOOH nanorods epitaxially grow along the normal direction of $(330)_{FeOOH}$ planes on the (10–1) surface of the SnO_2.[4] The parallel relationship between $(330)_{FeOOH}$ and $(10–1)_{SnO2}$ planes is supported by their fast Fourier transformation (FFT) patterns (insets in Figure 4b) and HRTEM image of the junction from another branched nanowire (Figure S2). For SnO_2 with tetragonal structure (a = b = 4.738 Å, c = 3.187 Å), the (101) plane and [101] direction are not perpendicular but inclined at an angle of 68°. The growth direction of the SnO_2 nanowires, angled 68° to the (101) plane, is determined to be [101].[20] The side surfaces of such SnO_2 nanowires can be further indexed as $\pm(010)_{SnO2}$ and $(10–1)_{SnO2}$ planes. Thus, the branches satisfying the above epitaxial relationship, namely $(330)_{FeOOH}//(10–1)_{SnO2}$, will grow along the $[110]_{FeOOH}$ direction and perpendicular to the stem, since ±(10–1) planes are parallel to the [101] direction in tetragonal SnO_2 (e.g., the growth direction of SnO_2 nanowires). More evidence of the perpendicular orientation of the branches is given by TEM images in Figure S3.

In addition to the above mentioned two groups of FeOOH branches perpendicular to the $(10–1)_{SnO2}$ plane, the other four groups of branches are observed to exhibit a slantwise growth mode on the rest two side faces of the SnO_2 stem, each forming 60° with respect to the stem (Figure S4). As the $(330)_{FeOOH}$ plane is parallel to $(10–1)_{SnO2}$ plane, the equivalent planes, $\pm(3–30)_{FeOOH}$, can be deduced to be parallel to $\pm(010)_{SnO2}$ planes. However, as schematically illustrated in Figure 4c, a perpendicular growth on the $\pm(010)_{SnO2}$ planes would result in a lattice mismatch as large as 47.7% [(0.474–0.248)/0.474 ≈ 47.7%]. Instead, when the branches grow slantwise, the interfacial lattice mismatch can be reduced to 4.6% [(0.496–0.474)/0.474 ≈ 4.6%] (Figure 4d). This implies that the branches have to grow at an inclined angle (e.g., 60°) in order to accommodate a thermodynamically stable epitaxial growth from the substrate. As a result, the growth mode of the branches on $\pm(010)_{SnO2}$ planes of the stem differs from that on the $\pm(10–1)_{SnO2}$ planes, leading to the formation of a six-fold orientation rather than four-fold. The adopted calculation methodology has also been used to

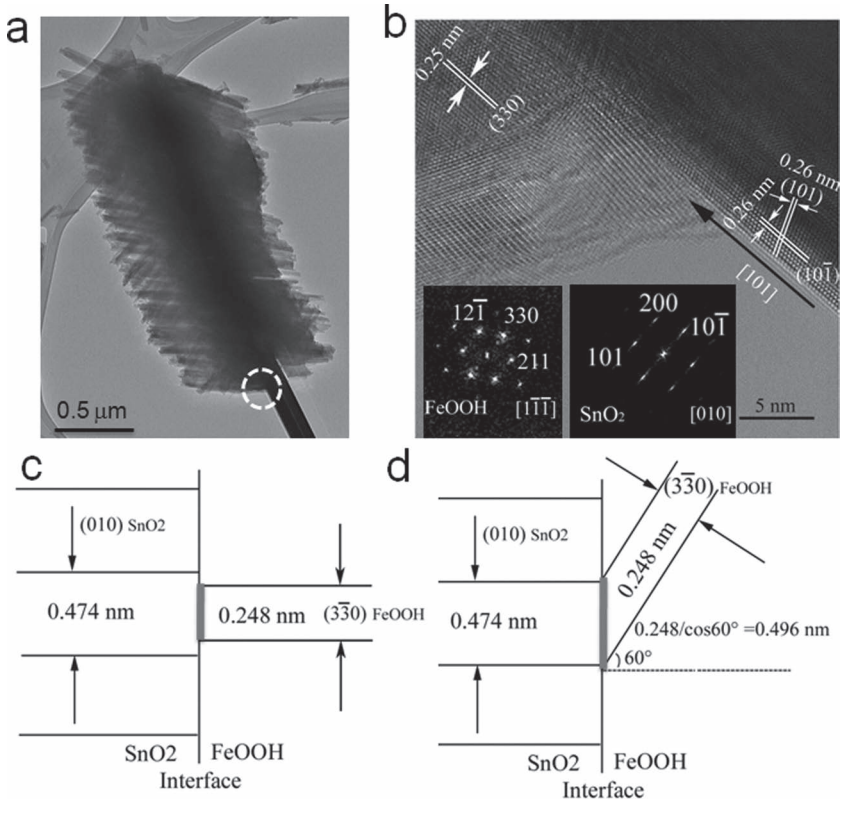

Figure 4. a) TEM image of FeOOH/SnO_2 branched nanostructure; b) High-resolution TEM image of the circular area in (a); insets are the fast Fourier transformation (FFT) patterns of the SnO_2 stem and FeOOH branch, respectively; c, d) Schematics of the interface of the $(010)_{SnO2}$ plane of SnO_2 stem and the $(3–30)_{FeOOH}$ plane of FeOOH branch, revealing the lower interfacial lattice mismatch of slantwise growth mode compared with that of perpendicular growth.

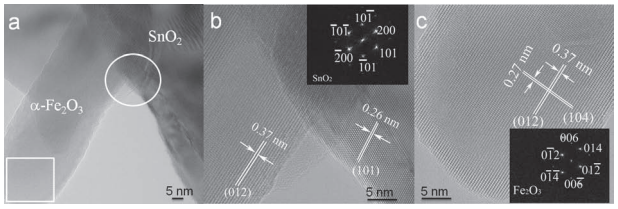

Figure 5. a) Low-magnification TEM image of the α-Fe_2O_3/SnO_2 branched nanostructure; b, c) Corresponding high-resolution TEM images of the circular and square areas in (a); insets are corresponding fast-Fourier transformation (FFT) patterns of the stem and branch.

explain the epitaxial relationships of the nano-heterostructures in other work.[4,21] According to above analysis, it is suggested that different preferential growth orientations of the FeOOH branches on distinct crystallographic surfaces of the SnO_2 stem are driven by the least interfacial lattice mismatches. It should be noted that most previously-proposed growth mechanisms for hierarchical nanostructures of similar six-fold symmetry are based on a hexagonal-shaped stem, which provides six equivalent planes to induce the secondary growth of the branches.[4,10b,11b,19,22] In our case, the core SnO_2 nanowires have only four exposed side facets. Therefore, the uniqueness herein is that the tetragonal core can induce a six-fold-symmetry growth of secondary branches. Meanwhile, the angles between the adjacent branches can be derived to be 60° as well, consistent with the SEM and TEM observations (Figure S5).

The structural characterization on the α-Fe_2O_3/SnO_2 obtained via post-annealing is presented in **Figure 5**a–c. Note that the interface epitaxial relationship has changed from $(330)_{FeOOH}//(10–1)_{SnO2}$ to $(012)_{\alpha\text{-}Fe2O3}//(101)_{SnO2}$ after annealing (Figure 5b). From the HRTEM image and corresponding FFT image of the branches (Figure 5c, inset), it is concluded that the α-Fe_2O_3 branches still exhibit a single-crystalline feature on the whole.

In order to have a closer inspection of the evolution processes of nanorod branches, samples at different reaction stages were collected. **Figure 6**a–f are the SEM images of the products obtained from various growth time, indicating the morphological and structural transformation from SnO_2 nanowires to α-Fe_2O_3/SnO_2 branched nanocomposites. After the initial 30 min reaction, there was no visible change to the bare tetragonal SnO_2 nanowires (Figure 6a). However, after another 30 min growth, nanoparticles of ~10 nm diameter nucleated on the surfaces of the SnO_2 nanowires were observed. These small nanoparticles exhibited a thorn-like shape, indicating the tendency of anisotropic growth (Figure 6b). When the reaction time was further prolonged to 2 h, the earlier-formed thorn-like nanoparticles elongated, establishing the rudiments of nanorods. Although a few branches already exhibited the symmetrical feature in this reaction stage (Figure S6), most backbone nanowires appeared to be surrounded by nanoparticles with different orientations (Figure 6c). However, by further increasing the reaction time to 4 h, hierarchical nanostructures of perfect six-fold-symmetry were formed with a branches length of about 250 nm (Figure 6d). After that, only the lengths of branches increased with an increase of the reaction time (350 nm for 10 h; 500 nm for 24 h), whereas the overall morphology showed no change (Figure 6e–f).

Based on the above analysis, we propose a simple three-step growth process as follows (Figure 6g). Firstly, through a hydrolyzation of $FeCl_3$ under acidic condition, the formed FeOOH nuclei attach to the SnO_2 nanowire surfaces and are oriented along the preferred direction of crystallization. Secondly, these particles grow into aligned nanorods with increasing time, resulting in six-fold-symmetry branches surrounding the SnO_2 nanowire stem. The basic theory and conditions for such an anisotropic growth have been elaborated in a previous report.[23] Finally, $FeOOH/SnO_2$ topologically transforms into α-Fe_2O_3/SnO_2 branched nanocomposite induced by the thermal annealing.

2.2. Function as Lithium-Ion Battery Anode

Recently, a worldwide effort has been made to search for superior LIBs anode materials to improve their energy density and safety.[17a, 24] Here we employ our α-Fe_2O_3/SnO_2 branched nano-heterostructures as the potential polymer binder-free anode material for LIBs as a comparison to pure α-Fe_2O_3 nanorods and SnO_2 nanowires. The lithium storage properties

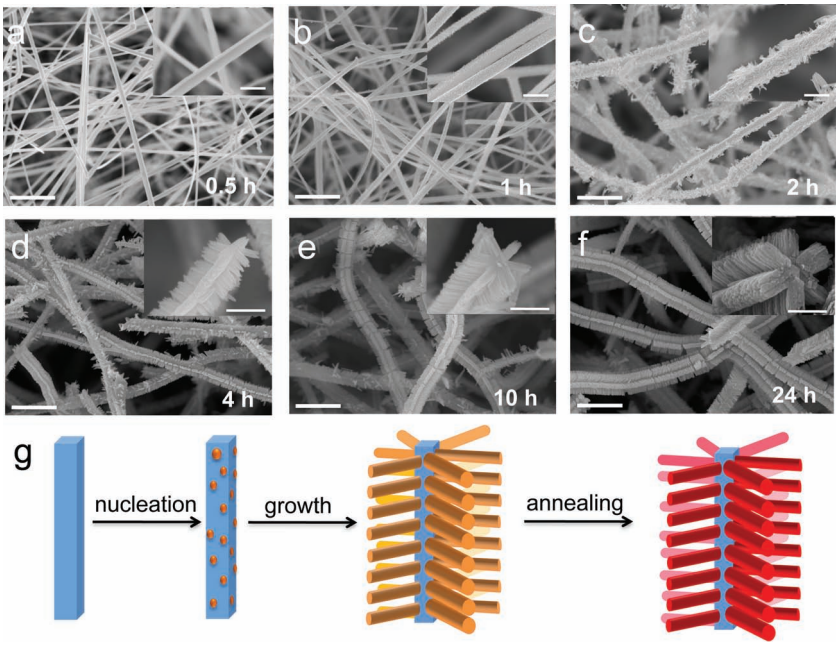

Figure 6. a–f) SEM images of the products (after annealing) at various reaction stages by setting the reaction time. The insets are the corresponding magnified SEM images. The scale bars in the figures and insets are 2 µm and 500 nm, respectively. g) Schematic of the formation process of the hierarchically assembled α-Fe_2O_3/SnO_2 nanocomposite.

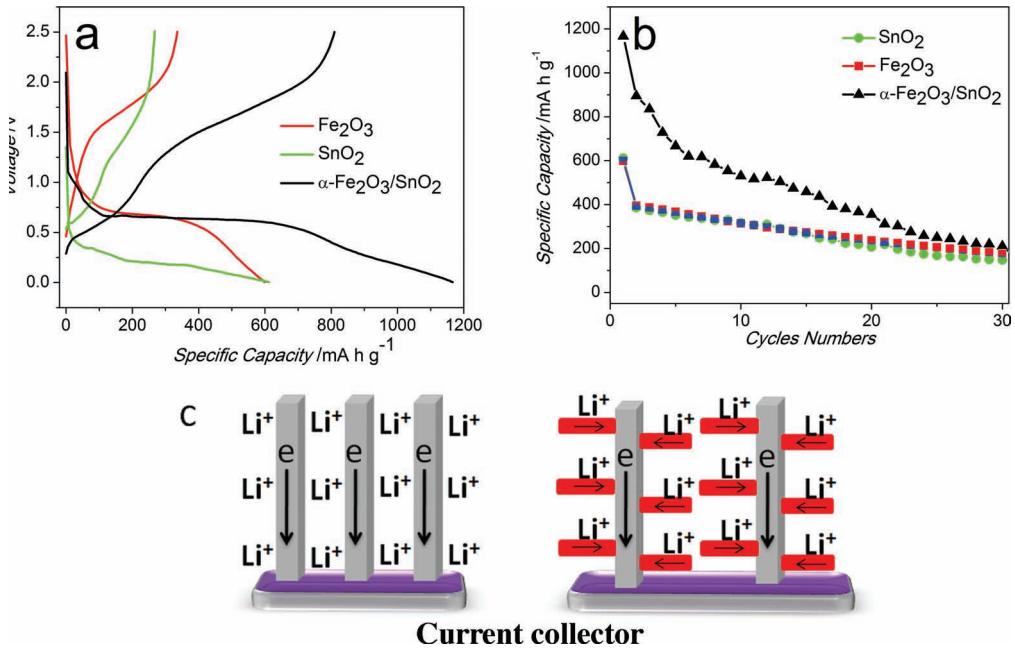

Figure 7. Application of the branched nanostructures as lithium-ion battery anodes. a) First charge-discharge profiles at a rate of 1000 mA g^{-1}. b) Cycling performance of bare α-Fe_2O_3 nanorod arrays, pristine SnO_2 nanowires, and α-Fe_2O_3/SnO_2 branched nanostructure. c) Schematic comparison of the unidirectional nanowires and branched nanostructures for electron collection. The latter provides more active surface sites for Li^+ access than the former, and thus delivers more electrons to the current collector.

of these α-Fe_2O_3/SnO_2 branched nano-heterostructures are electrochemically evaluated versus Li under galvanostatic condition at the current rate of 1000 mA g^{-1} in the potential window of 0.005–2.5 V. **Figure 7**a displays the first-cycle charge-discharge profile of α-Fe_2O_3/SnO_2 hierarchical nanostructure electrode and those of SnO_2 nanowires and α-Fe_2O_3 nanorods (The corresponding SEM images of the SnO_2 nanowires and α-Fe_2O_3 nanorods are shown in Figure S7). The branched nano-heterostructures show a remarkably improved initial discharge capacity of 1167 mA h g^{-1}, which is almost twice the SnO_2 nanowires (612 mA h g^{-1}) and α-Fe_2O_3 nanorods (598 mA h g^{-1}). Moreover, the composite electrode also exhibits the lowest initial irreversible loss of 30.6%, compared to 43.9% for α-Fe_2O_3 nanorods and 56.4% for SnO_2 nanowires. Herein, the much lower irreversible loss of our α-Fe_2O_3/SnO_2 branched nano-heterostructure can be attributed to a synergetic effect between SnO_2 and α-Fe_2O_3.[25] Specifically, in a SnO_2/Li half cell, there are two principle electrochemical processes:[17b,26]

$$SnO_2 + 4Li^+ + 4e^- \rightarrow Sn + 2Li_2O \quad (1)$$

$$Sn + xLi^+ + xe^- \leftrightarrow Li_xSn (0 \le x \le 4.4) \quad (2)$$

As for transition metal oxide α-Fe_2O_3, the electrochemical reaction mechanism with Li can be described by: $Fe_2O_3 + 6Li^+ + 6e^- \leftrightarrow 2Fe + 3Li_2O$, which is fully reversible.[27] It is noted that reversible formation and decomposition of the Li_2O nanomatrix could be electrochemically driven by the metal nanoparticles formed in situ. Hence, the presence of Fe nanoparticles at the interface between α-Fe_2O_3 and SnO_2 may improve the reversibility of the reaction (Equation 1) and further result in a higher reversible capacity. Therefore, branching SnO_2 with a transition metal oxide can be considered as an effective route to resolve one major drawback of SnO_2-based anode materials, namely, large initial irreversible loss. Figure 7b depicts the comparative cycling performance of these three samples up to 30 cycles. A large drop in capacity of second cycle is obviously seen for all the samples due to the initial irreversible loss. Despite the relatively faster capacity fading behaviour, the composite electrode always demonstrates higher capacity compared to the pristine SnO_2 nanowires and α-Fe_2O_3 nanorod arrays.

Since the composite electrode exhibits a higher capacity than both single components, the enhancement is not simply a result of the introduction of a higher capacity component. Instead, it more likely originates from the unique heterostructure of the composite electrode, which is elaborated as follows. On one hand, the enhanced capacity of branched nano-heterostructures compared with the bare SnO_2 nanowires can be easily understood by the addition of a higher capacity component α-Fe_2O_3 and the synergistic effect of α-Fe_2O_3 branches and SnO_2 stems mentioned above. Specifically, the α-Fe_2O_3 branches not only provide new Li^+ hosts but also increase the reversible capacity of SnO_2 by improving the reversibility of the reaction (shown in Equation 1). On the other hand, it is interesting to understand why the branched nano-heterostructures still show higher capacity than the pure α-Fe_2O_3 nanorod arrays since a lower-capacity component, SnO_2, is introduced. Herein, the reason can be the following: As can be seen from Figure S7a, when directly grown on conductive substrate, α-Fe_2O_3 nanorods have a very dense structure, which reduces the accessibility of the electrolyte (Li^+) for the electrochemical reactions. However,

after branching on the SnO_2 nanowires, the α-Fe_2O_3 nanorods have an increased portion of exposed surfaces and thus can provide more active sites for Li^+ ions accesses, as schematically demonstrated in Figure 7c. It can be easily observed from the SEM images of the branched nano-heterostructures that there are a lot of free spaces between the branched nanowires, which ensures a high utilization of electrode materials, and, thus, a high capacity. Furthermore, as the α-Fe_2O_3 nanorods are porous (see Figure S4, S6), the effect of the sparse arrangement on inducing high capacity will be stronger. Hence, the capacity increase arising from the higher α-Fe_2O_3 surface areas outweighs the capacity decrease resulting from the introduction of the lower-capacity component, SnO_2. As a result, the composite electrode still exhibits higher capacity than pure α-Fe_2O_3 nanorod arrays. Another factor that should be taken into account is that the branches may relieve the stress exerted on inner nanowires caused by severe volume change arising from alloying–dealloying process (reaction 2, shown in Equation 2) during the numerous charge–discharge cycles, and thus suppress the degradation of the core material. The effort to improve the capacity retention is ongoing.

3. Conclusions

A novel six-fold-symmetry branched α-Fe_2O_3/SnO_2 nano-heterostructure is prepared by hydrothermal growth of α-Fe_2O_3 precursor branches on pre-obtained SnO_2 nanowire stems. The uniqueness of the structure is that, the SnO_2 nanowire stems with four non-equivalent exposed side surfaces can give rise to six-fold-symmetry growth of FeOOH nanorod branches by accommodating different epitaxial orientations on distinct crystallographic surfaces. The lengths of branches can be effectively tuned by changing the reactant concentration or reaction time. In comparison to both single components, such a composite LIBs anode material has demonstrated superior electrochemical performance (e.g., lower initial irreversible loss and higher reversible capacity). The improvement could be ascribed to a synergetic effect between α-Fe_2O_3 and SnO_2 as well as the unique feature of branched nanostructures which provides increased specific surface areas. Such α-Fe_2O_3/SnO_2 composite might also find other applications such as photoelectrochemical water splitting and gas sensing.

4. Experimental Section

Sample Synthesis: The SnO_2 nanowires were presynthesized on stainless steels via a standard chemical vapor deposition method according to our previous publication.[14a] Then, the α-Fe_2O_3/SnO_2 hierarchical structures were prepared by a seed, catalyst, and surfactant-free hydrothermal method, the recipe of which was slightly modified from previous reports on preparation of α-Fe_2O_3 nanorod arrays.[23] In a typical process, a piece of stainless steel substrate covered by SnO_2 nanowires was placed within a 50 mL sealed Teflon autoclave containing a solution (30 mL) consisting of $FeCl_3.6H_2O$ (0.15 M) and $NaNO_3$ (1M), and the pH value adjusted to ~1.5 by hydrochloric acid (36.5%). The hydrothermal reaction was conducted at 100 °C for 24 h. After that, the substrate was removed from the solution, rinsed with deionized water, and dried with N_2 blow. Further heat treatment in air at 450 °C for 2 h is required for the phase transition from the resulting precursors (FeOOH) to pure α-Fe_2O_3. By replacing the stainless steel with Ti foil while other conditions keep unchanged, pure α-Fe_2O_3 nanorod arrays could be obtained.

Sample Characterizations: The morphology and the crystalline structure of the as-fabricated SnO_2/α-Fe_2O_3 nano-heterostructures were characterized with a JEOL JSM-6700F field emission scanning electron microscope (FE-SEM) and a JEM 2010F high-resolution transmission electron microscope (HR-TEM). X-ray powder diffraction (XRD) patterns were recorded on a Bruker D8 Advance diffractometer using Cu Kα radiation.

Electrochemical Measurement: The electrochemical tests were carried out using two-electrode cells with pure lithium metal as the counter and reference electrodes at room temperature. The α-Fe_2O_3/SnO_2 semiconductor branched nanostructures on stainless steel were directly used as working electrode. In order to get relatively reliable data of the sample mass, we used an AX/MX/UMX Balance (METTLER TOLEDO, Maximum = 5.1 g; d = 1 μg). The mass of the sample can be calculated after the subtraction of bare substrate's mass. For each sample, 10 pieces of 2 cm^2 substrates were measured before and after growth to get the statistical average mass. In comparison, the Li-ion batteries performance of pure SnO_2 nanowires and α-Fe_2O_3 nanorod arrays were also tested. The electrolyte used was $LiPF_6$ (1.0 M) in a mixture of ethylene carbonate and diethyl carbonate (1:1 by volume). The Swagelok-type cell assembly was carried out in an Ar-filled glovebox (Mbraun, Unilab, Germany) with concentrations of moisture and oxygen below 1.0 ppm. The discharge-charge cycling was performed at room temperature by using a multichannel battery tester (model SCN, USA).

Supporting Information

Supporting Information is available from the Wiley Online Library or from the author.

Acknowledgements

This work is partly supported by the Clean Energy Research Program (CERP, NRF2009EWT-CERP001–036) in NTU, Singapore.

Received: January 13, 2011
Revised: January 27, 2011
Published online: March 25, 2011

[1] a) H. G. Yang, H. C. Zeng, *J. Am. Chem. Soc.* **2004**, *127*, 270; b) L. Ouyang, K. N. Maher, C. L. Yu, J. McCarty, H. Park, *J. Am. Chem. Soc.* **2006**, *129*, 133; c) J. Y. Lao, J. G. Wen, Z. F. Ren, *Nano Lett.* **2002**, *2*, 1287; d) A. Cao, V. P. Veedu, X. Li, Z. Yao, M. N. Ghasemi-Nejhad, P. M. Ajayan, *Nat. Mater.* **2005**, *4*, 540; e) L. J. Lauhon, M. S. Gudiksen, C. L. Wang, C. M. Lieber, *Nature* **2002**, *420*, 57; f) R. Yang, Y.-L. Chueh, J. R. Morber, R. Snyder, L.-J. Chou, Z. L. Wang, *Nano Lett.* **2006**, *7*, 269; g) T. Y. Zhai, L. Li, X. Wang, X. S. Fang, Y. Bando and D. Golberg, *Adv. Funct. Mater.* **2010**, *20*, 4233.
[2] a) B. Sun, E. Marx, N. C. Greenham, *Nano Lett.* **2003**, *3*, 961; b) I. Gur, N. A. Fromer, C.-P. Chen, A. G. Kanaras, A. P. Alivisatos, *Nano Lett.* **2006**, *7*, 409.
[3] M. J. Bierman, S. Jin, *Energy & Environ Sci* **2009**, *2*, 1050.
[4] M. T. Niu, F. Huang, L. F. Cui, P. Huang, Y. L. Yu, Y. S. Wang, *ACS Nano* **2010**, *4*, 681.
[5] S. Zhou, X. Liu, D. Wang, *Nano Lett.* **2010**, *10*, 860.
[6] M. J. Bierman, Y. K. A. Lau, A. V. Kvit, A. L. Schmitt, S. Jin, *Science* **2008**, *320*, 1060.
[7] J.-K. Oh, J.-K. Lee, H.-S. Kim, S.-B. Han, K.-W. Park, *Chem. Mater.* **2009**, *22*, 1114.
[8] S. Mathur, S. Barth, *Small* **2007**, *3*, 2070.

[9] a) S. H. Sun, G. W. Meng, G. X. Zhang, J. P. Masse, L. Zhang, *Chem.-Eur. J.* **2007**, *13*, 9087; b) Z. L. Wang, Z. W. Pan, *Adv. Mater.* **2002**, *14*, 1029.

[10] a) M. T. Niu, Y. Cheng, Y. S. Wang, L. F. Cui, F. Bao, L. H. Zhou, *Cryst. Growth Des.* **2008**, *8*, 1727; b) D. F. Zhang, L. D. Sun, C. J. Jia, Z. G. Yan, L. P. You, C. H. Yan, *J. Am. Chem. Soc.* **2005**, *127*, 13492.

[11] a) J. Zhou, Y. Ding, S. Z. Deng, L. Gong, N. S. Xu, Z. L. Wang, *Adv. Mater.* **2005**, *17*, 2107; b) S. J. May, J. G. Zheng, B. W. Wessels, L. J. Lauhon, *Adv. Mater.* **2005**, *17*, 598; c) T. Y. Zhai, Z. J. Gu, H. Z. Zhong, Y. Dong, Y. Ma, H. B. Fu, Y. F. Li, J. N. Yao, *Cryst. Growth Des.*, **2007**, *7*, 488.

[12] a) J. Zhu, H. Peng, C. K. Chan, K. Jarausch, X. F. Zhang, Y. Cui, *Nano Lett.* **2007**, *7*, 1095; b) J. Zhu, H. Peng, A. F. Marshall, D. M. Barnett, W. D. Nix, Y. Cui, *Nat. Nanotechnol.* **2008**, *3*, 477.

[13] a) K. A. Dick, K. Deppert, M. W. Larsson, T. Martensson, W. Seifert, L. R. Wallenberg, L. Samuelson, *Nat. Mater.* **2004**, *3*, 380; b) Y. Jung, D.-K. Ko, R. Agarwal, *Nano Lett.* **2006**, *7*, 264.

[14] a) C. W. Cheng, B. Liu, H. Y. Yang, W. W. Zhou, L. Sun, R. Chen, S. F. Yu, J. X. Zhang, H. Gong, H. D. Sun, H. J. Fan, *ACS Nano* **2009**, *3*, 3069; b) K. Takahashi, S. J. Limmer, Y. Wang, G. Z. Cao, *J. Phys. Chem. B*, **2004**, *108*, 9795.

[15] H. Xie, Y. Z. Li, S. F. Jin, J. J. Han, X. J. Zhao, *J. Phys. Chem. C* **2010**, *114*, 9706.

[16] K. K. Khun, A. Mahajan, R. K. Bedi, *J. Appl. Phys.* **2009**, *106*, 124509.

[17] a) J. P. Liu, Y. Y. Li, H. J. Fan, Z. H. Zhu, J. Jiang, R. M. Ding, Y. Y. Hu, X. T. Huang, *Chem. Mater.* **2010**, *22*, 212; b) J. P. Liu, Y. Y. Li, X. T. Huang, R. M. Ding, Y. Y. Hu, J. Jiang, L. Liao, *J. Mater. Chem.* **2009**, *19*, 1859.

[18] Y. J. Chen, C. L. Zhu, L. J. Wang, P. Gao, M. S. Cao, X. L. Shi, *Nanotechnology* **2009**, *20*, 045502.

[19] W. C. Zhou, A. L. Pan, Y. Li, G. Z. Dai, Q. Wan, Q. L. Zhang, B. S. Zou, *J. Phys. Chem. C* **2008**, *112*, 9253.

[20] W.-S. Kim, D. Kim, K. J. Choi, J.-G. Park, S.-H. Hong, *Cryst. Growth Des.* **2010**, *10*, 4746.

[21] M. Casavola, V. Grillo, E. Carlino, C. Giannini, F. Gozzo, E. Fernandez Pinel, M. A. Garcia, L. Manna, R. Cingolani, P. D. Cozzoli, *Nano Lett.* **2007**, *7*, 1386.

[22] H. J. Fan, R. Scholz, F. M. Kolb, M. Zacharias, U. Gosele, F. Heyroth, C. Eisenschmidt, T. Hempel, J. Christen, *Appl. Phys. A: Mater. Sci. Process.* **2004**, *79*, 1895.

[23] L. Vayssieres, N. Beermann, S. E. Lindquist, A. Hagfeldt, *Chem. Mater.* **2001**, *13*, 233.

[24] a) S. J. Han, B. C. Jang, T. Kim, S. M. Oh, T. Hyeon, *Adv. Funct. Mater.* **2005**, *15*, 1845; b) Y. Li, B. Tan, Y. Wu, *Nano Lett.* **2007**, *8*, 265; c) C. K. Chan, R. N. Patel, M. J. O'Connell, B. A. Korgel, Y. Cui, *ACS Nano* **2010**, *4*, 1443; d) Y. Wang, G. Z. Cao, *Adv. Mater.* **2008**, *20*, 2251; e) C. K. Chan, H. L. Peng, G. Liu, K. McIlwrath, X. F. Zhang, R. A. Huggins, Y. Cui, *Nat. Nanotechnol.* **2008**, *3*, 31.

[25] J. S. Chen, C. M. Li, W. W. Zhou, Q. Y. Yan, L. A. Archer, X. W. Lou, *Nanoscale* **2009**, *1*, 280.

[26] a) M. S. Park, Y. M. Kang, G. X. Wang, S. X. Dou, H. K. Liu, *Adv. Funct. Mater.* **2008**, *18*, 455; b) X. W. Lou, J. S. Chen, P. Chen, L. A. Archer, *Chem. Mater.* **2009**, *21*, 2868.

[27] P. Poizot, S. Laruelle, S. Grugeon, L. Dupont, J. M. Tarascon, *Nature* **2000**, *407*, 496.